ORIGINAL PAPER

P. A. van Aken · B. Liebscher

Quantification of ferrous/ferric ratios in minerals: new evaluation schemes of Fe L_{23} electron energy-loss near-edge spectra

Abstract Determination of $Fe^{3+}/\Sigma Fe$ in minerals at submicrometre scale has been a long-standing objective in analytical mineralogy. Detailed analysis of energy-loss near-edge structures (ELNES) of the Fe L_{23} core-loss edges recorded in a transmission electron microscope (TEM) provides chemical information about the iron oxidation state. The valence-specific multiplet structures are used as valence fingerprints. Systematic investigations on the Fe L_{23} ELNES of mono and mixed-valence Fe-bearing natural minerals and synthetic solid solutions of garnets (almandine-skiagite and andradite-skiagite), pyroxenes (acmite-hedenbergite) and spinels (magnetite-hercynite) are presented where the presence of multiple valence states is distinguished by a splitting of the Fe L_3 edge. We demonstrate the feasibility of quantification of the ferrous/ferric ratio in minerals by analyzing the Fe L_{23} ELNES as a function of the ferric iron concentration resulting in three independent methods: (1) The method of the modified integral intensity ratio of the Fe L_{23} white lines employs two 2-eV-wide integration windows centring around both the Fe L_3 maximum for Fe^{3+} and the Fe L_2 maximum for Fe^{2+}. This refined routine, compared to the previously published quantification method of the ferrous/ferric ratio in minerals, leads to an improved universal curve with acceptable absolute errors of about ± 0.03 to ± 0.04 for $Fe^{3+}/\Sigma Fe$ ratios. (2) The second method uses a simple mathematical description of the valence-dependent splitting of Fe L_3 ELNES by fitting several Gaussian functions and an arctan function.

The systematic analysis of the integral portions of the individual Gaussian curves for different mineral groups provides a further $Fe^{3+}/\Sigma Fe$ quantification method with an absolute error of about ± 0.02 to ± 0.03. (3) The Fe L_3 ELNES can also be modelled with the help of reference spectra, whereby the $Fe^{3+}/\Sigma Fe$ ratio can be determined with an absolute error of ca. ± 0.02.

Keywords Ferrous/ferric ratios · Electron energy-loss spectroscopy (EELS) · Energy-loss near-edge structure (ELNES) · Transmission electron microscopy (TEM)

Introduction

The high spatial resolution available on a transmission electron microscope (TEM) combined with the benefits of electron energy-loss spectroscopy (EELS) allows detailed analysis of multivalent element ratios (e.g. Fe^{2+} and Fe^{3+}) on the scale of nanometres. Such data allow determination of redox states for mineral crystallization and interpretation of geological evolution of mineral reactions. Estimation of $P\text{-}T$ conditions of igneous and metamorphic rocks via geothermobarometers that involve $Fe^{2+}\text{-}Mg^{2+}$ exchange in coexisting minerals (e.g. Essene 1982; Luth et al. 1990; Canil and O'Neill 1996) and determination of oxygen fugacity (Frost 1991) can be significantly affected by neglecting Fe^{3+} or using incorrect values. Hence, the precise knowledge of the ferrous/ferric ratio in iron-bearing minerals is indispensable for the understanding of the exact crystal chemistry of constituent minerals.

Modern developments have had an enormous impact on the number and quality of $Fe^{3+}/\Sigma Fe$ quantification methods, including electron microprobe analysis (EPMA), Mössbauer spectroscopy, X-ray photoelectron (XPS) and X-ray absorption near-edge structure (XANES) spectroscopy, and EELS. Traditionally, the ferric iron concentration is estimated from elemental electron microprobe analysis by stoichiometric calculation, which, however, is restricted by uncertainties and

P. A. van Aken (✉)
Institut für Mineralogie der TU Darmstadt,
Schnittspahnstr. 9, 64287 Darmstadt
e-mail: vanaken@geo.tu-darmstadt.de
Tel.: + 49-6151-162180
Fax: + 49-6151-164021

B. Liebscher
Institut für Mineralogie der Universität Frankfurt,
Senckenberganlage 28, 60054 Frankfurt

assumptions (Canil and O'Neill 1996) and is extremely sensitive to errors since the analytical errors of all other element concentrations are combined in its calculation (Spear 1995). Recently, progress has been made in EPMA by the flank method (Höfer et al. 1994), which is based on the concomitant changes of both the intensity ratio and the wavelength of the Fe L_α and Fe L_β X-ray emission lines with $Fe^{3+}/\Sigma Fe$. This method was established for iron oxides (hematite, magnetite and wüstite), olivines and synthetic hercynite-magnetite solid solutions (Höfer et al. 1994) and for garnets (Höfer et al. 1995) – the same samples were used in this study – and has further been applied to $Fe^{3+}/\Sigma Fe$ determination of sodic amphiboles (Enders et al. 2000) and of wüstites synthesized at different oxygen fugacities (Höfer et al. 2000). Although relatively high spatial resolution can be obtained on the order of 1 μm, the results for $Fe^{3+}/\Sigma Fe$ are strongly influenced by carbon contamination and carbon coating, by peak shape alterations and by matrix correction procedures used in data analysis (Höfer et al. 2000). In general, it is accepted that $Fe^{3+}/\Sigma Fe$ ratios determined by Mössbauer spectroscopy of mineral separates are most accurate, but this technique has to be used as a bulk method with lower spatial resolution limited to ca. 200 μm (McCammon et al. 1991; McCammon 1994).

Advances in XPS (Raeburn et al. 1997a,b) provide another technique for quantitative analysis of $Fe^{3+}/\Sigma Fe$ which was shown for individual biotite crystals using the Fe $3p$ photoelectron peak. During the past decade, enormous progress has been made in the determination of $Fe^{3+}/\Sigma Fe$ ratios of iron-bearing silicates and iron oxides measuring XANES at the Fe K edge (Manceau et al. 1992; Sutton et al. 1993; Bajt et al. 1994; Delaney et al. 1996, 1998; Dyar et al. 1998; King et al. 2000) and at the Fe L_{23} edge (van der Laan and Kirkman 1992; Cressey et al. 1993; Crocombette et al. 1995). The spatial resolution obtainable in XPS and XANES lies between those of EPMA and Mössbauer spectroscopy, however, with a larger error in $Fe^{3+}/\Sigma Fe$ determination.

Fe L_{23} ELNES studies provide chemical information about valence-specific multiplet structures of iron which can be used as valence fingerprints. The Fe L_{23} edges are characterized by sharp maxima at the near-edge region, which are known as white lines. EELS spectra of Fe^{2+}- and Fe^{3+}-bearing minerals show distinct Fe L_{23} edge shapes and chemical shifts. Although transitions from the Fe $2p$ to $3d$ and $4s$ symmetry orbitals are allowed by the selection rule of dipole transition, the probability of transition to the s orbitals is much lower, and the Fe L_{23} spectra are dominated by excitation to Fe $3d$ orbitals. Transitions to the dipole-allowed s-like states have only a small effect on the Fe L_{23} edges and are manifested as weak structures at higher energies above the Fe L_{23} peaks (Abbate et al. 1992). The atomic state changes from the $2p^6 3d^n$ Fe ground state to the $2p^5 3d^{n+1}$ state after the excitation of a $2p$ core electron, where $n = 5$ for Fe^{3+} and $n = 6$ for Fe^{2+}. The L_3 and L_2 lines are transitions of $2p_{3/2}$ to $3d_{3/2} 3d_{5/2}$ and $2p_{1/2}$ to $3d_{3/2}$,

respectively, and their intensities are related to the unoccupied states in the $3d$ bands (van der Laan and Kirkman 1992). The two white-line features, L_3 and L_2, are separated by about 13 eV due to the spin-orbit splitting of the Fe $2p$ core hole. Nowadays, EELS investigations at the Fe L_{23} and Fe M_{23} edges with a TEM allow qualitative (Leapman et al. 1982; Otten et al. 1985; Krishnan 1990; Paterson and Krivanek 1990; Garvie et al. 1994) and detailed quantitative (van Aken 1995; Garvie and Buseck 1998; van Aken et al. 1998; 1999; Gloter et al. 2000a, b; Lauterbach et al. 2000; Liebscher 2000) analysis of $Fe^{3+}/\Sigma Fe$ ratios at highest spatial and high-energy resolution among all analytical microbeam methods. Furthermore, Golla and Putnis (2001) were able to record quantitative compositional maps and Fe^{3+}/Fe^{2+} valence state distribution maps at nanometre scale of hematite-ilmenite exsolutions in a natural titanohematite crystal using electron spectroscopic imaging in an energy-filtered TEM. Hence, one main objective of EELS aims at an improvement of the accuracy in $Fe^{3+}/\Sigma Fe$ determination.

In this paper, we present systematic investigations on the Fe L_{23} ELNES of mono and mixed valence Fe-bearing natural minerals and synthetic solid solutions of garnets (almandine-skiagite and andradite-skiagite), pyroxenes (acmite-hedenbergite) and spinels (magnetite-hercynite), where the presence of multiple valence states is distinguished by a splitting of the Fe L_3 edge. In particular, the method of $Fe^{3+}/\Sigma Fe$ determination using the universal curve (van Aken et al. 1998) was extended to pyroxenes, iron oxides and iron hydroxides, resulting in improved absolute errors of about ± 0.03 to ± 0.04. Another procedure employs a simple mathematical description of the valence-dependent splitting of Fe L_3 ELNES by fitting several Gaussian functions and an arctan function. The systematic analysis of the integral portions of the individual Gaussian curves for different mineral groups provides a further $Fe^{3+}/\Sigma Fe$ quantification method with an absolute error of about ± 0.02 to ± 0.03. An improvement of the approach by van Aken (1995) and Garvie and Buseck (1998) is proposed by modelling only the more intense Fe L_3 ELNES spectra, using reference spectra resulting in low absolute errors of ca. ± 0.02 for the deduced $Fe^{3+}/\Sigma Fe$ ratios. The accuracy and errors of the three methods are discussed and compared to previously published techniques.

Experimental methods, data evaluation and sample catalogue

The EELS experiments were performed at 120 kV using a Philips CM 12 TEM equipped with an energy-dispersive X-ray micro-analysis (EDX) system EDAX PV9900 and a Gatan 666 PEELS. The single-crystal LaB$_6$ cathode operated in an undersaturated mode produces a typical energy width of ca. 0.8 eV measured as full width at half maximum (FWHM) of the zero-loss peak. To ensure the validity of dipole selection rules for the electronic transitions from the $2p$ core level (Egerton 1996), the EELS spectra were acquired in the diffraction mode at small scattering angles under the following conditions: 0.1 eV/channel energy dispersion,

Table 1 Mineral name, simplified formula, $Fe^{3+}/\Sigma Fe$ and reference of the iron-bearing samples used in this study

Mineral and sample name	Simplified formula	$Fe^{3+}/\Sigma Fe$	Reference
Garnets			
Almandine–skiagite al–sk[(S)][a]: al$_{93}$sk$_7$, al$_{85}$sk$_{15}$, al$_{79}$sk$_{21}$, al$_{59}$sk$_{41}$, al$_{21}$sk$_{79}$, al$_{10}$sk$_{90}$	$Fe_3^{2+}Al_2[SiO_4]_3 - Fe_3^{2+}F_3^{2+}[SiO_4]_3$	0.045, 0.091, 0.123, 0.215, 0.345, 0.375	Woodland and O'Neill (1993), Woodland and Ross (1994)
Andradite–skiagite and–sk[(S)]: and$_{11}$sk$_{89}$, and$_{22}$sk$_{78}$, and$_{37}$sk$_{63}$, and$_{72}$sk$_{28}$, and$_{82}$sk$_{18}$, and$_{93}$sk$_7$	$Ca_3Fe_2^{3+}[SiO_4]_3 - Fe_2^{2+}Fe_2^{3+}[SiO_4]_3$	0.428, 0.461, 0.514, 0.704, 0.787, 0.905	Woodland and Ross (1994), Woodland and O'Neill (1995)
Andradite and$_{100}$[(S)]	$Ca_3Fe_2^{3+}[SiO_4]_3$	1.0	Synthesis Fehr, unpubl.
Almandine al$_{97}$[(N)]	$Fe_3Al_2[SiO_4]_3$	0.03	Woodland et al. (1995)
Andradite–grossular and$_{82}$gr$_{18}$[(N)][b]	$Ca_3(Fe^{3+},Al)_2[SiO_4]_3$	1.0	Tamnau collection, TU Darmstadt
Pyroxenes			
Hedenbergite–acmite hd–ac[(S)]: hd$_{100}$, ac$_{10}$hd$_{90}$, ac$_{25}$hd$_{75}$, ac$_{40}$hd$_{60}$, ac$_{50}$hd$_{50}$, ac$_{60}$hd$_{40}$, ac$_{75}$hd$_{25}$, ac$_{90}$hd$_{10}$, ac$_{100}$	$CaFe^{2+}[SiO_3]_2 - NaFe^{3+}[SiO_3]_2$	0.015, 0.099, 0.223, 0.384, 0.440, 0.572, 0.702, 0.898, 1.0	Redhammer (1996); Redhammer et al. (2000)
Hedenbergite hd$_{100}$[(N)]	$CaFe^{2+}[SiO_3]_2$	0.0	Tamnau collection, TU Darmstadt
Acmite ac$_{100}$[(N)]	$NaFe^{3+}[SiO_3]_2$	1.0	Tamnau collection, TU Darmstadt
Spinels			
Hercynite hc$_{100}$[(S)]	$Fe^{2+}Al_2O_4$	0.0	Synthesis Fockenberg, unpubl.
Hercynite–magnetite hc–mt[(S)]: hc$_{100}$, mt$_5$hc$_{95}$, mt$_{10}$hc$_{90}$, mt$_{20}$hc$_{80}$, mt$_{30}$hc$_{70}$, mt$_{40}$hc$_{60}$, mt$_{50}$hc$_{50}$, mt$_{60}$hc$_{40}$, mt$_{70}$hc$_{30}$, mt$_{100}$[(S)]	$Fe^{2+}Al_2O_4 - Fe^{3+}(Fe^{2+}Fe^{3+})O_4$	0.0, 0.091, 0.167, 0.286, 0.375, 0.444, 0.500, 0.545, 0.583, 0.667	Synthesis O'Neill, unpubl.
Spinel–magnetite sp$_{90}$mt$_{10}$[(S)]	$MgAl_2O_4 - Fe^{3+}(Fe^{2+}Fe^{3+})O_4$	0.667	Synthesis Woodland, unpubl.
Hercynite hc$_{100}$[(N)]	$Fe^{2+}Al_2O_4$	0.0	Tamnau collection, TU Darmstadt
Magnetite mt$_{100}$[(N)]	$Fe^{3+}(Fe^{2+}Fe^{3+})O_4$	0.667	Ramdohr collection, University of Heidelberg
Franklinite fr$_{100}$[(N)]	$ZnFe_2^{3+}O_4$	1.0	Tamnau collection, TU Darmstadt
Olivines			
Fayalite fa$_{100}$[(S)]	$Fe_2^{2+}SiO_4$	0.0	Synthesis Brey, unpubl.
Forsterite fo-54[(N)]	$(Mg,Fe^{2+})_2SiO_4$	0.0	Köhler and Brey (1990)
Forsterite fo-90[(N)]	$(Mg,Fe^{2+})_2SiO_4$	0.0	Köhler and Brey (1990)
Forsterite fo-91[(N)]	$(Mg,Fe^{2+})_2SiO_4$	0.0	Tamnau collection, TU Darmstadt
Iron oxides and hydroxides			
Wuestite: wu-20, wu-4, wu-15, wu-18, wu-14[(S)]	$Fe_{0.949}O$, $Fe_{0.935}O$, $Fe_{0.922}O$, $Fe_{0.910}O$, $Fe_{0.897}O$	0.11, 0.14, 0.17, 0.20, 0.23	Höfer et al. (2000)
Hematite[(N)]	Fe_2O_3	1.0	Tamnau collection, TU Darmstadt
Goethite[(N)]	$FeO(OH)$	1.0	Tamnau collection, TU Darmstadt
Other			
Brownmillerite[(S)]	$Ca_2Fe_2O_5$	1.0	Colville (1970)
Fe-orthoclase[(S)]	$KFeSi_3O_8$	1.0	Synthesis Shaw, unpubl.

[a] [(S)]: synthetic sample
[b] [(N)]: natural sample

2 mm PEELS entrance aperture, $\alpha = 2.6$ mrad illumination semi-angle, $\beta = 7$ mrad spectrometer acceptance semiangle. We examined 6–12 grains per sample measured at different crystal orientations to exclude errors due to orientation-dependent effects and sample inhomogenity and also to improve reproducibility. A wide range of measuring geometries including the TEM nanoprobe mode was used, which provides small spotsizes down to 10 nm and illumination of semiangles up to 10 mrad, although the standard measuring conditions for the Fe L_{23} spectra in the TEM diffraction mode use larger spotsizes on the order of 1 µm. This allows short measuring times of 30 s integration time. To improve the counting statistics, we always measured a series of at least six spectra to be added. This gives us a good control of possible changes in the specimen during the EELS investigations because we have to take care of and to avoid electron beam-induced chemical reactions as oxidation processes.

Data processing of the measured spectra includes corrections for channel-to-channel gain variations as well as for the dark current of the detector. Afterwards, the background intensity at the Fe L_{23} edges is subtracted by fitting an inverse power-law function for a range of 30–50 eV before the edge and extrapolating this function to higher energies. The Fe L_{23} core-loss ionization edges and the

corresponding low-loss valence EELS spectrum, including the zero-loss peak, were acquired consecutively from the same specimen region. The low-loss spectrum was used to remove the multiple-inelastic scattering effects in the core-loss region using the Fourier ratio technique (Egerton 1996). Consequently, the data presented here are the results of the single scattering processes.

We examined 54 natural and synthetic iron-bearing minerals, well characterized for chemical composition and ferric/ferrous ratio by electron microprobe analysis, Mössbauer spectroscopy and X-ray diffraction. Table 1 summarizes data on nomenclature, sample identification, $Fe^{3+}/\Sigma Fe$ and reference. TEM specimens are exclusively prepared by crushing small crystals between clean glass slides, and suspending tiny fragments with ethanol onto standard holey TEM grids. This procedure needs only very small amounts of sample material compared to ion milling techniques, and provides enough electron-transparent grains. In general, these samples need no carbon coating.

Results and discussion

Fe L_{23} energy-loss near-edge structure

Fe^{2+} and Fe^{3+} in minerals are most commonly octahedrally coordinated, although Fe in four- and eight-fold coordination is sometimes found. The Fe L_{23} edges from a number of reference minerals containing Fe^{2+} and Fe^{3+} in four-, six- and eight-fold coordination are shown in Fig. 1. They are almandine ($al_{97} - {}^{[8]}Fe^{2+}$), hedenbergite ($hd_{100} - {}^{[6]}Fe^{2+}$), hercynite ($hc_{100} - {}^{[4]}Fe^{2+}$), the Fe analogue of orthoclase ($KFeSi_3O_8 - {}^{[4]}Fe^{3+}$), brownmillerite ($Ca_2Fe_2O_5 - {}^{[4+6]}Fe^{3+}$) and andradite ($and_{100} - {}^{[6]}Fe^{3+}$). The comparison of Fe L_{23} ELNES for different iron oxidation states already allows qualitative statements about the valence (Otten et al. 1985; van Aken et al. 1998; Garvie et al. 1994; Garvie and Buseck 1998; Krishnan 1990; Liebscher 2000;), since the Fe L_{23} edges show different edge shapes, as well as a distinct chemical shift between divalent and trivalent Fe L_{23} edges. The measured separation of the Fe L_3 and L_2 maxima, due to spin-orbit splitting of 12.8 ± 0.1 eV and 13.2 ± 0.1 eV for Fe^{2+} and Fe^{3+}, respectively, is in good agreement with previously published data (Colliex et al. 1991; Garvie et al. 1994; van Aken et al. 1998; Gloter et al. 2000a). The Fe^{2+} L_3 edges display a sharp maximum at 707.8 eV and a weaker partially resolved feature post the main maximum at around 710.5 eV, which is more distinct for ${}^{[8]}Fe^{2+}$ and ${}^{[6]}Fe^{2+}$. For Fe^{3+}-bearing compounds, the Fe L_3 edge shows a chemical shift of 1.7 eV with the main maximum at 709.5 eV. Andradite contains ${}^{[6]}Fe^{3+}$ and has a characteristic Fe L_3-edge shape, with a prepeak at 708.0 eV leading the main L_3 peak, whereas the Fe analogue of orthoclase, which contains ${}^{[4]}Fe^{3+}$, shows an L_3 edge without any pronounced fine structure. For ${}^{[6]}Fe^{3+}$- and ${}^{[4]}Fe^{3+}$-bearing brownmillerite, the prepeak at 708.0 eV is much weaker compared to andradite, suggesting that the Fe L_3 edge is composed of and can be described by a super-position of ${}^{[6]}Fe^{3+}$ and ${}^{[4]}Fe^{3+}$ L_3-edge spectra. The two peaks on the Fe L_3 edge in and_{100} are separated by 1.5 eV, as in many other ${}^{[6]}Fe^{3+}$-containing minerals, and have been assigned to $2p \rightarrow 3d$ transitions into t_{2g}

and e_g orbitals using a simple crystal-field model (Krishnan 1990). As a consequence, different site symmetries are documented by changes in the multiplet structures on the Fe L_3 edges. This effect, however, is, for example for the Ti L_{23} edges, much more dramatic. The spectral features of the Ti L_{23} ELNES are significantly influenced by the coordination and site symmetry of the Ti cation (de Groot et al. 1992), which was also shown for Ti^{4+}-bearing compounds in the coordinations $Ti^{[4]}$, $Ti^{[5]}$ and $Ti^{[6]}$ by Langenhorst and van Aken (2000).

Representative Fe L_3 ELNES spectra corrected for the continuum background (cf. subsequent section Total integral white-line intensity ratio) of the solid solutions of garnets (almandine-skiagite and skiagite-andradite) pyroxenes (hedenbergite-acmite) and spinels (hercynite-magnetite) containing various $Fe^{3+}/\Sigma Fe$ ratios are shown in Fig. 2a–c, respectively. The Fe L_3 edges of al_{97} (Fig. 2a) and hd_{100} (Fig. 2b) display their main maximum at 707.8 eV followed by a less intense maximum at ca. 710.5 eV. With increasing ferric iron concentration,
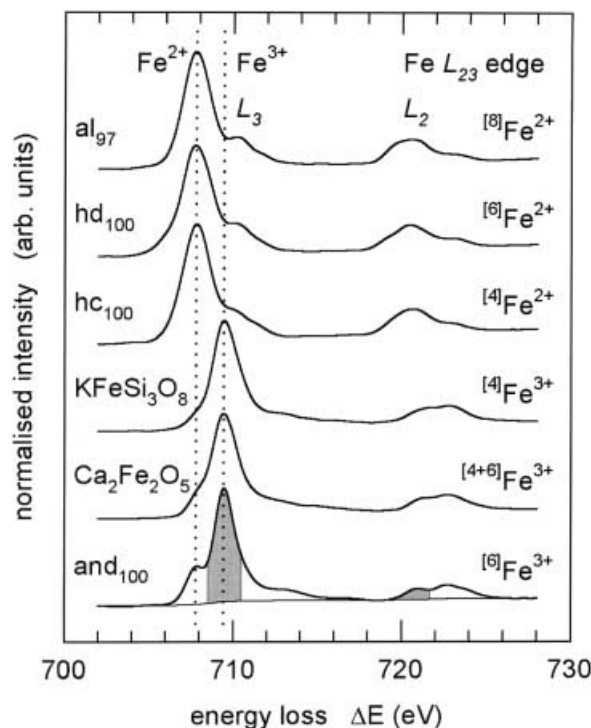

Fig. 1 Fe L_{23} edges from selected minerals containing single-valent Fe with different coordination numbers for Fe bonded to oxygen show a constancy of edge shape for given oxidation states: almandine ($al_{97} - {}^{[8]}Fe^{2+}$), hedenbergite ($hd_{100} - {}^{[6]}Fe^{2+}$), hercynite ($hc_{100} - {}^{[4]}Fe^{2+}$), Fe analogue of orthoclase ($KFeSi_3O_8 - {}^{[4]}Fe^{3+}$), brownmillerite ($Ca_2Fe_2O_5 - {}^{[4+6]}Fe^{3+}$) and andradite ($and_{100} - {}^{[6]}Fe^{3+}$). The spectra have been normalized to the integral Fe L_3-edge intensity, and some of the spectra have been shifted vertically for clarity. The *dotted lines* represent the position of the Fe L_3 white-line maxima located at 707.8 and 709.5 eV for Fe^{2+} and Fe^{3+}, respectively. The *solid line* below the Fe L_{23} edge of and_{100} represents the double arctan background function, and the *grey shaded areas* correspond to the integral intensities used for the $Fe^{3+}/\Sigma Fe$ quantification by applying the universal curve
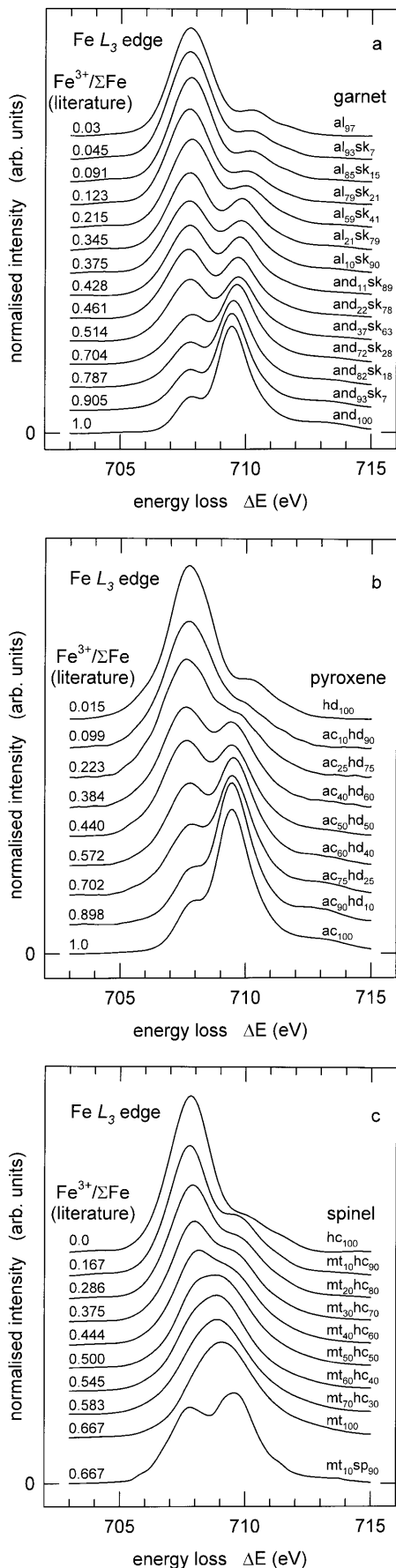
the relative intensity of the first peak decreases and the second peak at around 709.5 eV becomes more intense. For the Fe^{3+}-bearing end members and_{100} and ac_{100}, the maxima are located at 709.5 eV, with an additional peak at 708.0 eV. These basic edge shapes are consistent with published Fe L_3 ELNES (Colliex et al. 1991; Garvie et al. 1994; Garvie and Buseck 1998; Krishnan 1990, Paterson and Krivanek 1990; van Aken et al. 1998; Liebscher 2000) and Fe L_3 XANES (van der Laan and Kirkman 1992; Cressey et al. 1993; Crocombette et al. 1995). Accordingly, Fe L_3 spectra with iron in mixed valence states always show two separate Fe L_3 maxima for ferrous and ferric iron. The intensity ratios of these maxima are obviously dependent on ferric iron concentration, and the mean iron valence can be obtained by comparison with experimental standard spectra based on a simple valence fingerprint technique. Exceptions to this approach are the Fe L_3 ELNES of magnetite and magnetite-rich hercynite solid solutions (Fig. 2c). Their Fe L_3 spectra exhibit only one asymmetric peak due to strong charge-transfer interactions between ferrous and ferric iron on adjacent octahedral sites, which is known as electron hopping (e.g. Crocombette et al. 1995). With increasing magnetite concentration and a concomitant increase of $Fe^{3+}/\Sigma Fe$, the mt-hc Fe L_3 spectra show a systematic change from a spectrum with two peaks towards the magnetite spectrum with $Fe^{3+}/\Sigma Fe = 0.667$ displaying only one broad peak. A dramatic Fe L_3 edge alteration occurs when magnetite is highly diluted with common $MgAl_2O_4$ spinel ($mt_{10}sp_{90}$), while $Fe^{3+}/\Sigma Fe = 0.667$ remains constant. For $mt_{10}sp_{90}$, the iron cations on the octahedral sites are mainly neighboured to octahedral sites occupied with aluminium. Consequently, electron-hopping processes are frozen in, leading to the lowest Fe L_3 spectrum shown in Fig. 2c. The $mt_{10}sp_{90}$ Fe L_3 ELNES consists of two separate maxima located at 707.8 and 709.5 eV, which is very similar to the spectra for garnets and pyroxenes.

Total integral Fe L_{23} white-line intensity ratio

The anomalous behaviour of the L_3:L_2 white-line intensity ratios for all 3d transition metals was recognized in the early 1980s (Leapman et al. 1982). These intensity ratios show large valence-dependent deviations from the expected value of 2:1, in accordance with the multiplicity of the initial states with four $2p_{3/2}$ and two $2p_{1/2}$ electrons. This leads to the possibility of identifying the occupation number of the 3d orbital and concomitantly the 3d transition metal valence state. To establish

◄

Fig. 2a–c Fe L_3 ELNES normalized with respect to the integral intensity and corrected for the arctan background function of **a** the garnet solid solutions almandine-skiagite (*al-sk*) and andradite–skiagite (*and–sk*) and the natural garnet al_{97} **b** the pyroxene solid solutions acmite–hedenbergite (*ac–hd*) and **c** the spinel solid solutions magnetite–hercynite (mt–hc) and magnetite–spinel ($mt_{10}sp_{90}$). The $Fe^{3+}/\Sigma Fe$ ratios are data from literature (cf. Table 1).

the numerical proportionality between the white-line intensity ratio and the ferric iron concentration $Fe^{3+}/\Sigma Fe$, the white lines must be isolated from the background intensity which is due to transitions to unoccupied continuum states. Therefore, a double arctan function (Eq. 1) is used as a background function which is plotted in Fig. 1 for andradite.

$$f(\Delta E) = \frac{h_1}{\pi} \cdot \left[\arctan\left(\frac{\pi}{w_1} \cdot (\Delta E - E_1)\right) + \frac{\pi}{2}\right] + \frac{h_2}{\pi}$$
$$\times \left[\arctan\left(\frac{\pi}{w_2} \cdot (\Delta E - E_2)\right) + \frac{\pi}{2}\right] . \quad (1)$$

The height of the two arctan functions (h_1 and h_2) are scaled to the minima behind the Fe L_3- and the Fe L_2 edge with fixed inflection points at $E_1 = 708.65$ eV and $E_2 = 721.65$ eV and with fixed widths of $w_1 = w_2 = 1$ eV, which can be applied to all measured spectra in a consistent way. After subtracting this arctan function, the spectra are normalized to their total integral intensity to compare directly the near-edge structures.

Figure 3 shows the total integral Fe L_{23} white-line intensity ratios $I(L_3)/I(L_2)_{\text{tot}}$ as a function of the ferric iron content $Fe^{3+}/\Sigma Fe$. The values for the intensity ratios, increasing from about 3.7 for ferrous iron to about 5.5 for ferric iron, are in the same range as in previously published data. Small differences between the absolute values for our intensity ratios and the data of Colliex et al. (1991) depend on the model chosen for the isolation of the white lines from the underlying transitions to unoccupied continuum states, which affects the magnitude of the intensity fraction attributed to the continuum below the white-line peaks. An un-
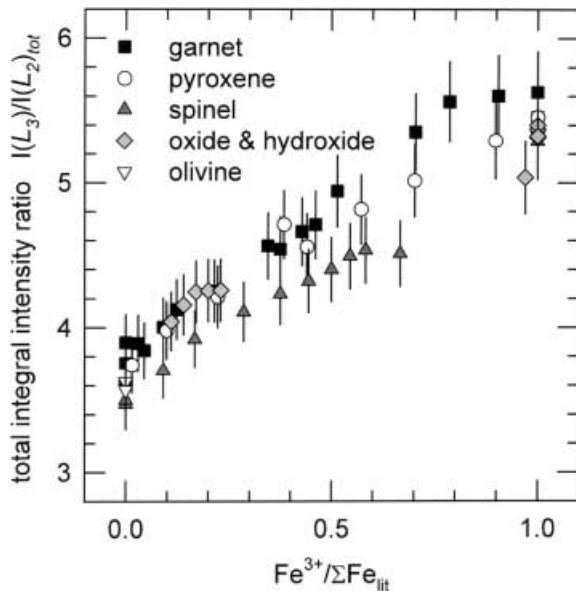
ambiguous variation of the total integral Fe L_{23} white-line intensity ratios with increasing $Fe^{3+}/\Sigma Fe$ occurs for the different minerals, and at first-order approximation, the data for different mineral groups can be described by a linear relationship which could be used for quantitative determination of ferric iron concentrations, however, with high absolute errors of ± 0.10 to ± 0.15. These results reveal that the total integral Fe L_{23} white-line intensity ratios are not only dependent on the iron valence state, but they also might be influenced by the crystal structure, e.g. coordination, and/or by the chemical composition. Although the L_{23} ELNES of four-, six-, and eightfold-coordinated iron exhibit only slight differences, we observe clear changes in the intensity ratios $I(L_3)/I(L_2)_{\text{tot}}$. For example, these values increase from 3.5 for tetrahedral coordinated Fe^{2+} to 3.6–3.7 for octahedral-coordinated Fe^{2+} and to 3.8–3.9 for eightfold-coordinated ferrous iron.

Modified integral Fe L_{23} white-line intensity ratio

The relatively small range for the total integral intensity ratios with a statistic standard deviation on the order of 5% of the absolute values causes relative high errors in the determination of $Fe^{3+}/\Sigma Fe$. Therefore, a modified method was developed in order to evaluate the intensity ratios, for which the continuum background was represented by the double arctan function, as defined in the previous section (Eq. 1), and subtracted from the Fe L_{23} ELNES. Furthermore, two integration windows of 2 eV width each were applied to the Fe L_{23} edges from 708.5 to 710.5 eV and from 719.7 to 721.7 eV centred around the maximum at the L_3 edge for Fe^{3+} and at the L_2 edge for Fe^{2+}, respectively, as previously described by van Aken et al. (1998). The modified integral white-line intensity ratios $I(L_3)/I(L_2)_{\text{mod}}$ of the pyroxene solid solution were used to test the validity of and to refine the universal curve, for which the results are shown in Fig. 4. The complete dataset is within the errors in good agreement with the calibration curve which can be described by a second-order hyperbolic function (Eq. 2)

$$\frac{I(L_3)}{I(L_2)_{\text{mod}}} = \frac{1}{a \cdot x^2 + b \cdot x + c} - 1 , \quad (2)$$

where $I(L_3)/I(L_2)_{\text{mod}}$ is the modified intensity ratio, x the ferric iron concentration $Fe^{3+}/\Sigma Fe$. The new parameters are $a = 0.193 \pm 0.007$, $b = -0.465 \pm 0.009$ and $c = 0.366 \pm 0.003$, and the coefficient of determination, r^2, is 0.9985. Within error limits, these values are identical to the previously published values (van Aken et al. 1998). The statistic standard deviation of the $I(L_3)/I(L_2)_{\text{mod}}$ ratios is less than 5%. This leads to acceptable absolute errors of about ± 0.03 to ± 0.04 for the determination of $Fe^{3+}/\Sigma Fe$ ratios, which will be discussed later in the section Error evaluation and error sources. The universal curve can be applied to the quantitative determination of $Fe^{3+}/\Sigma Fe$ without knowledge of sample composition or crystal structure, since the modified intensity ratios for all

Fig. 3 Total integral white-line intensity ratio $I(L_3)/I(L_2)_{\text{tot}}$ versus ferric iron concentration $Fe^{3+}/\Sigma Fe_{\text{lit}}$ for the solid solutions almandine–skiagite, skiagite–andradite, acmite–hedenbergite and hercynite–magnetite, as well as for iron oxides, hydroxides and olivines. The subscript *lit* refers to data taken from the literature

the measured samples (garnets, spinels, pyroxenes, iron oxides and hydroxides, olivines, cf. Table 1) are well described within the experimental errors. The compounds studied in this paper always contain iron in high-spin configuration which is bonded to oxygen atoms, as only strong field ligands cause spin pairing (e.g. Marfunin 1979). Low-spin Fe L_{23} edges display different spectral features as compared to their high-spin counterparts, e.g. in spin-transition compounds, $I(L_3)/I(L_2)$ can be modified with temperature where $Fe^{3+}/\Sigma Fe$ is constant (Briois et al. 1995). Therefore, the universal curve described here is restricted to compounds with iron in high-spin configuration.

Mathematical description of the Fe L_3 edge

In an effort to analyze the fingerprints of the Fe L_3 ELNES quantitatively with the intention of extracting the $Fe^{3+}/\Sigma Fe$ ratio, we developed a simple empirical model for the mathematical description of the Fe L_3-edge spectra. This model uses a sum of Gaussian functions in order to describe the spectral features and an arctan function to fit the remainder of the spectrum removing the contribution from transitions to the atomic continuum. The spectra were then fitted to Eq. (3):

Fig. 4 Modified integral white-line intensity ratio $I(L_3)/I(L_2)_{mod}$ versus ferric iron concentration $Fe^{3+}/\Sigma Fe$ using the 2-eV integration windows for garnets, pyroxenes, spinels, oxides, hydroxides and olivines. The resulting universal curve can be described by a second-order hyperbolic function (*solid line*). The *dotted lines* represent the error range with $\Delta(Fe^{3+}/\Sigma Fe) = \pm 0.03$

$$f(\Delta E) = \frac{h}{\pi} \cdot \left\{ \arctan\left[\frac{\pi}{w} \cdot (\Delta E - E_w)\right] + \frac{\pi}{2} \right\} + \sum_{i=1}^{i=4} H_i$$
$$\times \exp\left[-\frac{(\Delta E - E_i)^2}{W_i^2} \right] . \tag{3}$$

The arctan function was constrained to be zero at low energies but with following adjustable parameters: step height h, slope w describing the spectral resolution and position of the inflection point E_w resulting in an energy near the edge onset. The four Gaussian lines consist of the variables peak height H_i, peak position E_i and full width at half maximum (FWHM) W_i.

We make no attempt at assigning these fitted peaks to specific electronic absorptions. The purpose of this analytical fitting procedure is merely to quantify the previously described fingerprint technique in order to determine $Fe^{3+}/\Sigma Fe$ ratios. Hence, these Gaussian lines do not directly reflect the physical conditions, e.g. empty $3d$ states, but this technique is a useful tool in the description of the details of the Fe L_3 ELNES-like intensities, energy positions and FWHM of the visible maxima and spectral features. This model can be applied to spectra with iron in a single- or mixed-valence state, where several discrete peaks at the Fe L_3 edge appear. For the garnet solid solution series, the Gaussian lines used for the mathematical model and the fitted curve, which is in perfect agreement with the corresponding experimental Fe L_3-edge spectra, are shown in Fig. 5. Obviously, the intensity distribution of the individual Gaussian lines changes with increasing ferric iron concentration, and the integral intensity of the first peak at 707.8 eV systematically decreases with increasing $Fe^{3+}/\Sigma Fe$ (Fig. 5). This leads to a further possibility of determining $Fe^{3+}/\Sigma Fe$ ratios. Figure 6 shows the linear relationship between $x = Fe^{3+}/\Sigma Fe$ and the relative intensity of the first peak

$$y = \left(I_1 \bigg/ \sum_{i=1}^{i=4} I_i \right) \cdot 100\%$$

in the Fe L_3 ELNES, which is the integral intensity of the first peak normalized to the total integral intensity of the four Gaussian lines. This linear correlation $y = a \cdot x + b$ with $a = -68.4 \pm 0.7$ and $b = 83.1 \pm 0.4$ can be used for $Fe^{3+}/\Sigma Fe$ determination with absolute errors of about ± 0.02 to ± 0.03, and the coefficient of determination, r^2, is 0.997. The error estimation is discussed in more detail in the later section Error evaluation and error sources. However, this method has some restrictions and limitations, since for the fitting procedure very high-quality Fe L_3-edge spectra are required in terms of energy resolution and count statistics. Furthermore, electron-hopping processes, as in magnetite-rich spinel solid solutions (cf. Fig. 2c), cause smearing and blurring of the spectral features, so that the Fe L_3 ELNES consists of only one broad maximum, and hence, the mathematical description as presented above fails.
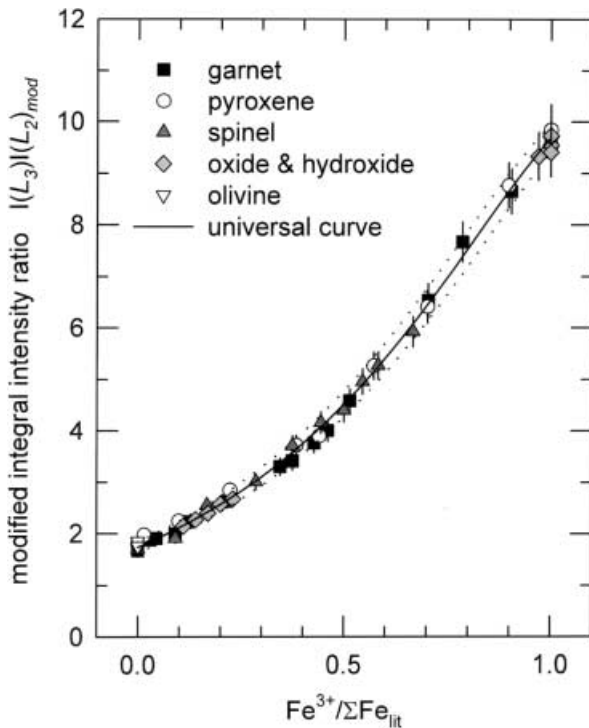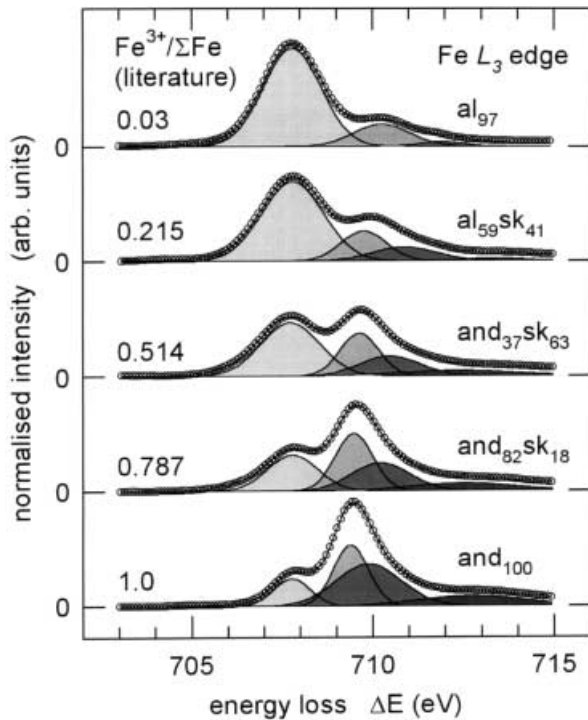
Fig. 5 The Fe L_3 ELNES of the garnets (al_{97}, $al_{59}sk_{41}$, $and_{37}sk_{63}$, $and_{82}sk_{18}$, and and_{100}) have been fitted in the range from 700 eV to the first minimum post the Fe L_3 white line to an arctan step function and four Gaussian lines. The diagram contains the experimental data (*circles*), the fitted curve (*solid line through the circles*) and the four different Gaussian lines (*grey shaded peaks*)

Regression with standard spectra

Since the Fe^{2+} and Fe^{3+} L_3 edges are well separated in energy, it is possible to determine $Fe^{3+}/\Sigma Fe$ ratios by fitting reference spectra to the experimental Fe L_{23} edges. This has been demonstrated by Cressey et al. (1993) using spectral simulations representing mixtures of Fe d^5 and Fe d^6 states as reference spectra and fitting them to the Fe L_{23} XANES from a number of phases (spinel, amphibole, Fe-containing glass and amethyst). Van Aken (1995) and Garvie and Buseck (1998) applied this method successfully to Fe L_{23} ELNES by fitting experimental reference spectra. Any Fe L_3 spectrum $M(\Delta E)$ can be described as a linear combination of two reference spectra $S_1(\Delta E)$ and $S_2(\Delta E)$ from samples with known $Fe^{3+}/\Sigma Fe$ ratios according to Eq. (4):
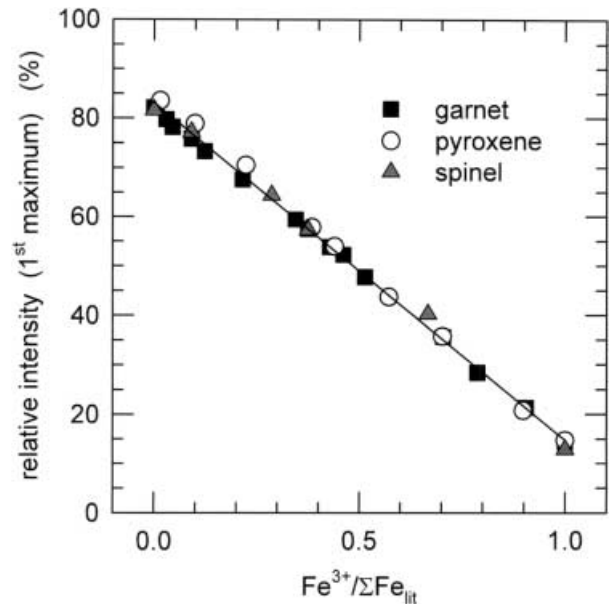

Fig. 6 Linear relationship between the relative integral intensity of the first peak 707.8 eV with respect to the integral intensity of all four Gaussian lines versus $Fe^{3+}/\Sigma Fe_{lit}$ for garnets, spinels and pyroxenes. The *solid line* is the linear best fit for the data

(Eq. 1). Garvie and Buseck (1998) used a straight line with a positive slope between 705 and 730 eV instead, which is an empirical assumption without physical basis, since the intensity of $2p$ electron excitations to unoccupied continuum states can be described in a first-order approximation as a step function. Furthermore, with increasing energy loss, the scattering cross-section of these transitions decreases and does not increase linearly. The procedure presented here uses two parameters, a and b, where the Fe L_3 reference spectra normalized to their integral intensity are fitted to the normalized Fe L_3 spectrum of the phase with unknown $Fe^{3+}/\Sigma Fe$ ratio. We restricted the fitting range to the Fe L_3 edge only, from 703 to 717 eV, in order to minimize the deviation between the $Fe^{3+}/\Sigma Fe$ ratio determined from the fitting procedure and the published value. The unknown $Fe^{3+}/\Sigma Fe(M)$ ratio of a sample can be calculated from the parameters a and b following Eq. (5), where $Fe^{3+}/\Sigma Fe(S_1)$ and $Fe^{3+}/\Sigma Fe(S_2)$ are the ferric iron concentrations of the reference compounds.

$$\frac{M(\Delta E)}{\int_{\Delta E=703eV}^{\Delta E=717eV} M(\Delta E)d(\Delta E)} = a \cdot \frac{S_1(\Delta E)}{\int_{\Delta E=703eV}^{\Delta E=717eV} S_1(\Delta E)d(\Delta E)} + b \cdot \frac{S_2(\Delta E)}{\int_{\Delta E=703eV}^{\Delta E=717eV} S_2(\Delta E)d(\Delta E)} \quad . \tag{4}$$

For the fitting procedure, the d-like component of the spectrum, representing the Fe L_3 white line, must be isolated from the continuum background intensity applying an arctan function as defined in the section above Total integral Fe L_{23} white-line intensity ratio

$$\frac{Fe^{3+}}{\Sigma Fe}(M) = \frac{a}{a+b} \cdot \frac{Fe^{3+}}{\Sigma Fe}(S_1) + \frac{b}{a+b} \cdot \frac{Fe^{3+}}{\Sigma Fe}(S_2) \tag{5}$$

The quality of this fitting procedure largely depends on the constancy of the Fe L_3-edge shapes in different

materials and environments. Since a large set of standard samples for different mineral groups was available, reference spectra were always chosen from the same mineral group as the compound with unknown $Fe^{3+}/\Sigma Fe$ ratio. Figure 7a,b illustrates typical examples, where the Fe L_3 spectrum of the garnet $and_{37}sk_{63}$ with $Fe^{3+}/\Sigma Fe = 0.514$ (published value, cf. Table 1 and Fig. 1a) is fitted with the garnet reference spectra of al_{97} and and_{100} (Fig. 7a) and of $and_{22}sk_{78}$ and $and_{72}sk_{28}$ (Fig. 7b). Although the residuals in Fig. 7a are quite large, the energy position and height of the maxima in the spectral analysis procedure are described well by the reference spectra, resulting in $Fe^{3+}/\Sigma Fe = 0.537$ with a goodness of fit of $r^2 = 0.967$ and $\chi^2 = 4.96$. These results are improved enormously when reference spectra of compounds with similar chemical composition and $Fe^{3+}/\Sigma Fe$ are used in the fitting procedure as in Fig. 7b, where the difference $\Delta(Fe^{3+}/\Sigma Fe) = 0.015$ between the calculated ferric iron concentration of $Fe^{3+}/\Sigma Fe = 0.529$ and the published value is smaller than in Fig. 7a. $\Delta(Fe^{3+}/\Sigma Fe) = 0.023$. Furthermore, the residuals are effectively minimized, which is expressed by an improved goodness of fit of $r^2 = 0.998$ and $\chi^2 = 0.16$. Thus, minerals with Fe^{2+} and Fe^{3+} show Fe L_3 spectra that are linear combinations of the separate Fe^{2+} and Fe^{3+} L_3 spectra, thereby allowing $Fe^{3+}/\Sigma Fe$ to be determined. For all investigated samples and mineral groups, we find
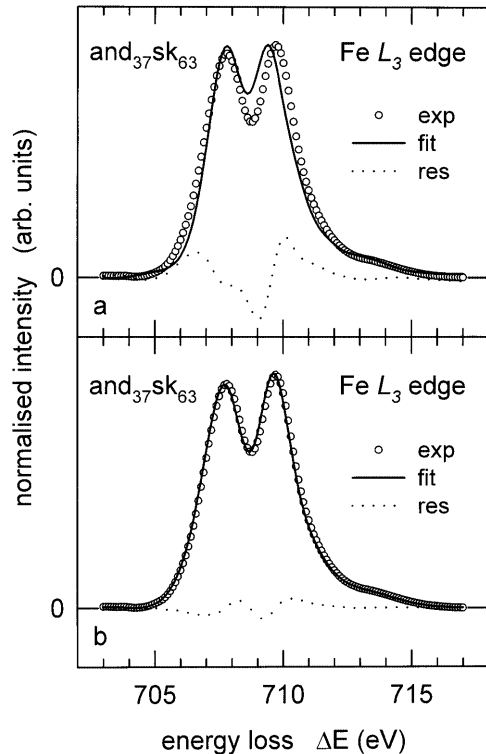
a very good agreement between the expected and calculated $Fe^{3+}/\Sigma Fe$ ratios with average deviations between $\Delta(Fe^{3+}/\Sigma Fe) = 0.01 - 0.02$. These deviations are smaller by a factor of 5 to 10 than the procedure used to determine $Fe^{3+}/\Sigma Fe$ ratios proposed by Garvie and Buseck (1998), since they have observed maximum absolute deviations of $\Delta(Fe^{3+}/\Sigma Fe) = 0.1$.

Error evaluation and error sources

The results of the $Fe^{3+}/\Sigma Fe$ determination by the three independent Fe L_{23} EELS analysis procedures (universal curve, peak fitting and fitting of reference spectra) are shown in Figs. 8 and 9a–c. For the error evaluation in $Fe^{3+}/\Sigma Fe$ determination, the Fe L_{23} spectra of all standard samples were used for both calibration and estimation of errors. In Fig. 8, the $Fe^{3+}/\Sigma Fe$ ratios determined by EELS and the published $Fe^{3+}/\Sigma Fe$ data are compared for which the data points lie on or at least very close to the 1:1 correlation line. In order to evaluate the absolute error in $Fe^{3+}/\Sigma Fe$ determination for the three different methods, the residuals between the calculated and published $Fe^{3+}/\Sigma Fe$ values, defined as $\Delta(Fe^{3+}/\Sigma Fe) = |Fe^{3+}/\Sigma Fe_{EELS} - Fe^{3+}/\Sigma Fe_{lit}|$, are shown in Fig. 9a–c. The smallest errors are obtained for the reference spectra fitting method (Fig. 9a), where the maximum deviation from the published value is $\Delta(Fe^{3+}/\Sigma Fe) = 0.022$. The mean value of $\Delta(Fe^{3+}/\Sigma Fe)$ is 7.5×10^{-3}, with a statistical standard deviation of 7.5×10^{-3} as indicated in Fig. 9a by the solid and dotted lines, respectively. Although the highest deviation for the peak fitting procedure amounts to about
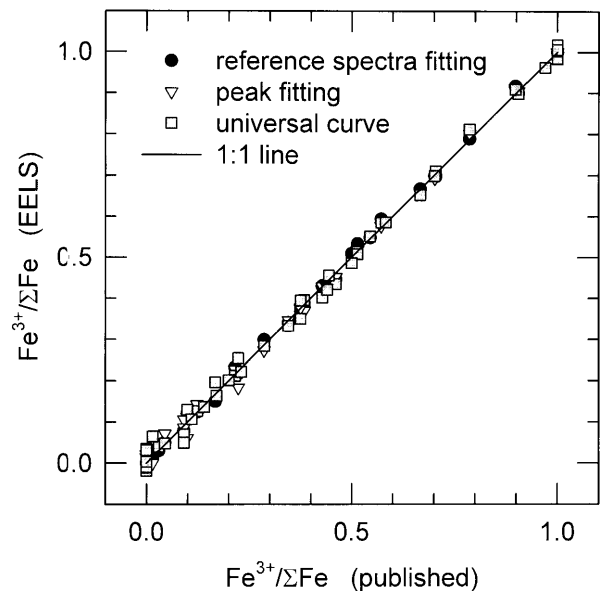
Fig. 7a, b The experimental Fe L_3 spectrum of $and_{37}sk_{63}$ (*circles*), the corresponding fit (*solid lines*) using the Fe L_3 spectra **a** of al_{97} and and_{100}, and **b** of $and_{22}sk_{78}$ and $and_{72}sk_{28}$ as reference spectra, and the differences between the experimental and fitted spectra (*dotted lines*) are superimposed at the same scale

Fig. 8 Comparison of $Fe^{3+}/\Sigma Fe$ ratios determined by the three independent Fe L_{23} EELS analysis procedures (universal curve, peak fitting and reference spectra fitting) and published results (cf. Table 1). All data lie within the errors on the 1:1 correlation line

$\Delta(Fe^{3+}/\Sigma Fe) = 0.04$ (Fig. 9b), the mean value and the standard deviation of $\Delta(Fe^{3+}/\Sigma Fe)$ are in an acceptable range, with 0.012 ± 0.011. The application of the universal curve exhibits the largest differences for $\Delta(Fe^{3+}/\Sigma Fe)$ with a maximum of 0.05 and a mean value of 0.015 ± 0.012 (Fig. 9c). The last method was performed for all investigated samples, instead of the first two procedures, where only the Fe L_3 ELNES of garnet, pyroxene and spinel samples were analyzed. Although the errors are slightly higher in the use of the universal curve, this method is a straightforward way to determine $Fe^{3+}/\Sigma Fe$ ratios, since no reference spectra have to be measured and no complicated fitting procedures have to be performed. The universal curve can be used for the quantitative determination of $Fe^{3+}/\Sigma Fe$ ratios without knowledge of sample composition or crystal structure. Hence, materials as diverse as extremely fine-grained materials like clay minerals in environmental sciences, or microstructure assemblages, like exsolutions and inclusions in petrology, and also the ferric iron characterization in amorphous materials (e.g. glasses) can be studied, since the crystallinity of the mineral has little effect on the shape of the Fe $L_{2,3}$ edges (Cressey et al. 1993; Garvie et al. 1994).
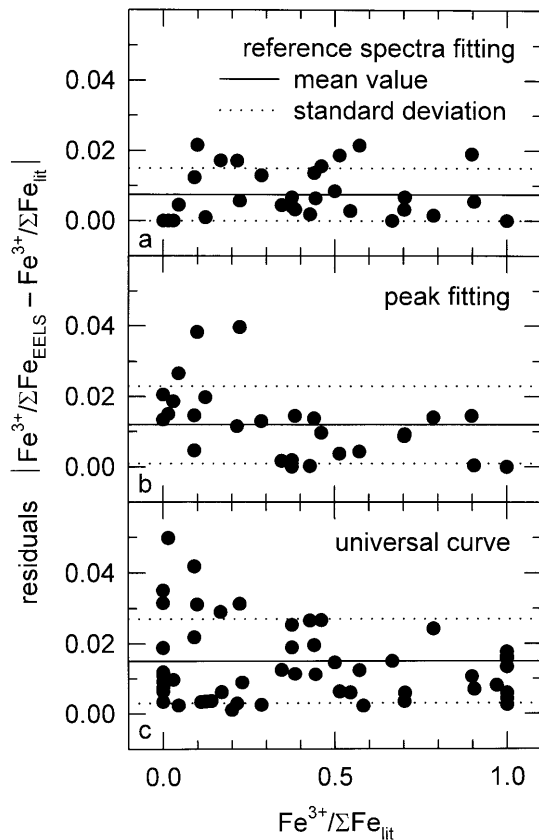

Fig. 9a–c Comparison of the residuals $|Fe^{3+}/\Sigma Fe_{EELS}-Fe^{3+}/\Sigma Fe_{lit}|$ with $Fe^{3+}/\Sigma Fe_{lit}$ for the three $Fe^{3+}/\Sigma Fe$ quantification procedures: **a** fitting of reference spectra, **b** peak fitting and **c** universal curve. The mean value (*solid lines*) and the statistical standard deviation (*dotted lines*) are shown for the three methods

Sources of error in the determination of $Fe^{3+}/\Sigma Fe$ ratios are difficult to eliminate, since they include the available energy resolution of the Fe L_{23} ELNES which is determined by TEM-EELS system, the signal-to-noise ratio of the spectra, possible beam damage of the sample and the mathematical treatment of the data (subtraction of the background, deconvolution of the multiple scattering, removal of the continuum background intensity under the Fe L_{23} white lines and the method for the determination of $Fe^{3+}/\Sigma Fe$ ratios itself). Furthermore, Gloter et al. (2000a) observed orientation-dependent effects of the Fe L_{23} egdes of aluminium-doped brownmillerite, which they interpreted as natural linear dichroism caused by internal axial components of the crystal field of octahedrally coordinated Fe^{3+}. Due to this dichroic observation, they questioned the accuracy of quantitative methods to measure ferrous/ferric ratios (Garvie and Buseck 1998; van Aken et al. 1998), since the specific effect of dichroism on the $Fe^{3+}/\Sigma Fe$ calculation reaches 16% for $Ca_2(Al_{0.67}Fe_{0.33})_2O_5$ (Table II in Gloter et al. 2000a). We will, however, demonstrate here that it is possible to overcome this problem.

Linear dichroism

Since its prediction by Thole et al. (1985) and observation by van der Laan et al. (1986), XAS dichroism has proved to be an impressive tool in the characterization of anisotropic materials. In linear dichroism, the absorption of linearly polarized radiation varies between two contrasting directions. It is commonly observed in anisotropic crystals, where the site symmetry of e.g. $3d$ transition metals is decreased and the charge distribution associated with the transition metal cation becomes distorted. Natural linear dichroism can be present in the absence of a magnetic exchange field, reflecting anisotropy of the ground state $3d$ charge distribution due to crystal-field interaction (see, e.g. Schofield et al. 1998 and references therein). Magnetic linear dichroism is used to determine the magnetic moment of $3d$ transition metals and rare earth ions in (anti)ferromagnetic and ferromagnetic materials (see, e.g. van der Laan et al. 1986; Kuiper et al. 1993). XAS linear dichroism is generally defined as the difference of the spectra $\Delta I = I_{\perp} - I_{||}$, where $I_{\perp}$ and $I_{||}$ are the spectra collected with polarization perpendicular and parallel to the principal axis, respectively.

In EELS, the situation differs slightly from XAS, since an electron energy-loss spectrum consists of excitations with the electron momentum transfer q parallel and perpendicular to the incident electron beam direction, whereby the relative weight of the two contributions depends on the experimental conditions α, β and θ_E. α and β are the convergence and collection semi-angles, respectively, and θ_E is the characteristic inelastic scattering angle (Egerton 1996). In EELS, the measured spectrum $I(\varphi)$ at a tilt angle φ between the principal axis, e.g. crystallographic c axis, and the incident electron

beam direction is a linear combination of $I_\perp$ and $I_\parallel$ (e.g. Menon and Yuan 1999). A comparison of the measured Fe L_{23} ELNES for scattering geometries with $\varphi = 0°$ and $\varphi = 90°$ (cf. Fig. 6a and b in Gloter et al. 2000a) leads to the maximum dichroism signal which can be observed in EELS. The spectra for $\varphi = 0°$ (Eq. 6a) and $\varphi = 90°$ (Eq. 6b), respectively, can be decomposed as:

$$I(\varphi = 0°) = \omega \cdot I_\parallel + (1 - \omega) \cdot I_\perp \tag{6a}$$

$$I(\varphi = 90°) = \omega \cdot I_\perp + (1 - \omega) \cdot (I_\perp + I_\parallel)/2 \ , \tag{6b}$$

where ω is the proportion of transitions with q parallel to the incident electron beam direction, the so-called parallel weighting fraction. Thus, the EELS linear dichroism ΔI (Eq. 7) can be written as

$$\Delta I = I(\varphi = 0°) - I(\varphi = 90°)$$
$$= (1 - 3 \cdot \omega) \cdot (I_\perp - I_\parallel)/2 \ , \tag{7}$$

and the resulting dichroism signal is only a part of the maximum difference spectrum attainable in XAS linear dichroism $(I_\perp - I_\parallel)$. In order to obtain an isotropic measurement of the Fe L_{23} ELNES and to determine "isotropic" $Fe^{3+}/\Sigma Fe$ ratios, Eq. (7) predicts the use of experimental conditions with $\omega = 1/3$. Gloter et al. (2000a) write in their manuscript: "... Nevertheless, the illumination conditions required to achieve this value are inadequate for a nanometre-scale analysis, and then cannot be used." This statement, however, is not correct, as will be pointed out in the following paragraph.

For our experimental conditions, i.e. $\alpha = 2.6$ mrad, $\beta = 7.0$ mrad and an energy loss of $\Delta E = 710$ eV at an incident electron beam energy of $E_0 = 120$ keV with a concomitant characteristic scattering angle for the Fe L_{23} edge of $\theta_E = 3.3$ mrad, the parallel weighting fraction ω is calculated for variable tilt angles φ using Eqs. (9a–c) and (10) from Menon and Yuan (1998).
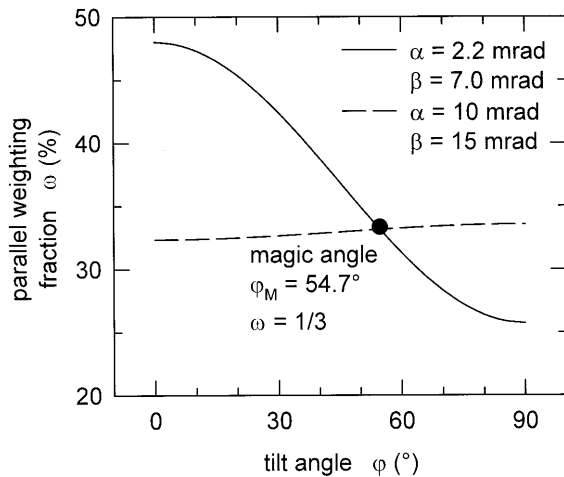
Under these experimental conditions, the parallel weighting fraction reaches its maximum value with $\omega = 48\%$ for $\varphi = 0°$ and decreases to $\omega = 26\%$ for $\varphi = 90°$ (solid line in Fig. 10). At a magic tilt angle of $\varphi_M = 54.7°$ between the principal axis and the incident electron beam direction, the parallel weighting fraction becomes $\omega = 1/3$, and hence, the Fe L_3 ELNES, measured at $\varphi_M = 54.7°$, corresponds to an isotropic spectrum. This geometric relation has already been described for isotropic XAS measurements by van der Laan et al. (1986) and Schofield et al. (1998). Table II in Gloter et al. (2000a) describes the $Fe^{3+}/\Sigma Fe$ ratio for $Ca_2(Al_{0.67}Fe_{0.33})_2O_5$ as a function of tilt angle φ with the **c** direction, where $Fe^{3+}/\Sigma Fe = 0.95–0.91$ for $\varphi = 45°$ and $Fe^{3+}/\Sigma Fe = 0.90$ for $\varphi = 60°$. The $Fe^{3+}/\Sigma Fe$ ratio determined by the isotropic Fe L_{23} edge yielded 0.91 (Table I in Gloter et al. 2000a). This value is located between the two $Fe^{3+}/\Sigma Fe$ ratios determined at $\varphi = 45°$ and 60°, and corresponds to an $Fe^{3+}/\Sigma Fe$ ratio determined from an Fe L_{23} spectrum measured at the magic angle $\varphi_M = 54.7°$. As a consequence, in the case of highly anisotropic materials, the dichroic effect can be minimized or becomes zero, when the isotropic Fe L_{23} ELNES is measured at this magic angle, in order to determine the "isotropic" $Fe^{3+}/\Sigma Fe$ ratio. This procedure, however, requires the exact knowledge of the crystallographic directions where maximum dichroic effect can be observed. Hence, for an unknown sample, it will be necessary to make several orientation-dependent measurements in order to exclude or minimize possible dichroism. Another possibility to minimize or overcome dichroistic effects is to increase the illumination and acceptance semiangles α and β. For example, if the semiangles are chosen as $\alpha = 10$ mrad and $\beta = 15$ mrad, then the parallel weighting fraction is calculated to $\omega(\varphi = 0°) = 0.32338$ and $\omega(\varphi = 90°) = 0.33536$ (dashed line in Fig. 10) with only minor deviation from the value for an isotropic spectrum ($\omega = 1/3$). Under these measuring conditions, one also would obtain an "isotropic" Fe L_{23} spectrum.

Fig. 10 Parallel weighting fraction ω as a function of tilt angle φ between the incident electron beam direction and the principal axis for following experimental conditions: *solid line* $\alpha = 2.6$ mrad, $\beta = 7.0$ mrad; *dotted line* $\alpha = 10$ mrad, $\beta = 15$ mrad and $\theta_E = 3.3$ mrad. At the magic angle $\varphi_M = 54.7°$ (*black dot*), the parallel weighting fraction is $\omega = 1/3$

Conclusions

We have shown that the EELS fine structures of the Fe L_{23} edges are largely controlled by the valency state of iron and, to a lesser extent, by the coordination number. A detailed experimental Fe L_{23} ELNES investigation of synthetic solid solutions of garnets, pyroxenes and spinels, as well as of a large number of natural and other synthetic samples (cf. Table 1), allows qualitative distinction between ferrous and ferric iron by means of Fe L_{23}-edge fingerprints. We have presented different methods for quantitative determination of $Fe^{3+}/\Sigma Fe$ ratios using the various details of the Fe L_{23} near-edge structures.

The total integral $L_3:L_2$ white-line intensity ratios display only small differences for ferrous and ferric iron, resulting in high absolute errors for the $Fe^{3+}/\Sigma Fe$

determination of about ± 0.10 to ± 0.15. The method of the modified integral intensity ratio of the Fe L_{23} white lines employing two 2-eV-wide integration windows leads to a universal behaviour for all investigated samples and mineral groups, resulting in acceptable absolute errors of about ± 0.04 for $Fe^{3+}/\Sigma Fe$ ratios. Another method employs a simple mathematical modelling of the valence-dependent splitting of Fe L_3 ELNES by fitting several Gaussian functions and an arctan function. The systematic analysis of the integral portions of the individual Gaussian curves for different mineral groups provides a further $Fe^{3+}/\Sigma Fe$ quantification method, with an absolute error of about ± 0.02 to ± 0.03. The linear regression with Fe L_3 reference spectra yields the best results, with the lowest absolute errors in $Fe^{3+}/\Sigma Fe$ of ± 0.02.

Once the $Fe^{3+}/\Sigma Fe$ ratio is determined from the universal curve, two optimum reference spectra can be chosen among the large set of Fe L_3 ELNES spectra of the investigated samples, where the $Fe^{3+}/\Sigma Fe$ ratio of the unknown sample lies between the values of the reference samples and the chemical compositions of the reference and unknown samples are nearly identical. As a consequence, this method becomes the most powerful tool for the quantitative determination of $Fe^{3+}/\Sigma Fe$ ratios. Anisotropic effects and orientation dependence of Fe L_{23} ELNES spectra, like natural linear dichroism in brownmillerite (Gloter et al. 2000a) and magnetic linear dichroism in hematite (Menon and Yuan 1999), can be minimized or even become zero, when the spectra are measured at the magic angle $\varphi_M = 54.7°$ between the principal axis and the incident electron beam direction, in order to obtain "isotropic" $Fe^{3+}/\Sigma Fe$ ratios.

References

Abbate M, de Groot FMF, Fuggle JC, Fujimori A, Strebel O, Lopez F, Domke M, Kaindl G, Sawatzky GA, Takano M, Takeda Y, Eisaki H, Uchida S (1992) Controlled-valence properties of $La_{1-x}Sr_xFeO_3$ and $La_{1-x}Sr_xMnO_3$ studied by soft X-ray absorption spectroscopy. Phys Rev (B)46: 4511–4519

Bajt S, Sutton SR, Delaney JS (1994) Microanalysis of iron oxidation states in silicates and oxides using X-ray absorption near-edge structure (XANES). Geochim Cosmochim Acta 58:5209–5214

Briois V, Cartier dit Moulin Ch, Sainctavit Ph, Brouder Ch, Flank AM (1995) Full multiple-scattering and crystal-field multiplet calculations performed on the spin transition $Fe^{II}(phen)_2$ $(NCS)_2$ complex at the iron K and $L_{2,3}$ X-ray absorption edges. J Am Chem Soc 117: 1019–1026

Canil D, O'Neill HStC (1996) Distribution of ferric iron in some upper mantle assemblages. J Petrol 37: 609–635

Colliex C, Manoubi T, Ortiz C (1991) Electron-energy-loss-spectroscopy near-edge fine structures in the iron-oxygen system. Phys Rev (B)40: 11402–11411

Colville AA (1970) The crystal structure of $Ca_2Fe_2O_5$ and its relation to the nuclear electric field gradient at the iron sites. Acta Crystalogr (B)26: 1469–1473

Cressey G, Henderson CMB, van der Laan G (1993) Use of L-edge X-ray absorption spectroscopy to characterize multiple valence states of $3d$ transition-metals; a new probe for mineralogical and geochemical research. Phys Chem Miner 20: 111–119

Crocombette JP, Pollak M, Jollet F, Thromat N, Gautier-Soyer M (1995) X-ray absorption spectroscopy at the Fe L_{23}-threshold in iron oxides. Phys Rev (B)52: 3143–3150

de Groot FMF, Figueiredo MO, Basto MJ, Abbate M, Petersen H, Fuggle JC (1992) $2p$ X-ray absorption of titanium in minerals. Phys Chem Miner 19: 140–147

Delaney JS, Bajt S, Sutton SR, Dyar MD (1996) In situ microanalysis of $Fe^{3+}/\Sigma Fe$ in amphibole by X-ray absorption near-edge structure (XANES) spectroscopy. In: Dyar MD, McCammon CA, Schaefer MW (eds) Mineral spectroscopy: a tribute to Roger G Burns. Geochem Soc Spec Publ 5: 175–171

Delaney JS, Dyar MD, Sutton SR, Bajt S (1998) Redox ratios with relevant resolution: solving an old problem by using the synchrotron microXANES probe. Geology 26: 139–142

Dyar MD, Delaney JS, Sutton SR, Schaefer MW (1998) Fe^{3+} distribution in oxidized olivine: a synchrotron micro-XANES study. Am Mineral 83: 1361–1365

Egerton RF (1996) Electron energy-loss spectroscopy in the electron microscope, 2nd edn. Plenum Press, New York

Enders M, Speer D, Maresch MV, McCammon CA (2000) Ferric/ferrous iron ratios in sodic amphiboles: Mössbauer analysis, stoichiometry-based model calculations and the high-resolution microanalytical flank method. Contrib Mineral Petrol 140: 135–147

Essene EJ (1982) Geologic thermometry and barometry. In: Ferry JM (ed) Characterization of metamorphism through mineral equilibria. Reviews in Mineralogy, vol. 10. Mineralogical Society of America, Washington, pp 153–206

Frost BR (1991) Introduction to oxygen fugacity and its petrologic importance. In: Lindsley, DH (ed) Oxide minerals: petrologic and magnetic significance. Reviews in Mineralogy, vol. 25. Mineralogical Society of America. Washington, pp 1–9

Garvie LAJ, Buseck PR (1998) Ratios of ferrous to ferric iron from nanometre-sized areas in minerals. Nature 396: 667–670

Garvie LAJ, Craven AJ, Brydson R (1994) Use of electron energy-loss near-edge fine structures in the study of minerals. Am Mineral 79: 411–425

Gloter A, Ingrin J, Bouchet D, Colliex C (2000a) Composition and orientation dependence of the O K and Fe $L_{2,3}$ EELS fine structures in $Ca_2(Al_xFe_{1-x})_2O_5$. Phys Rev (B)61: 2587–2594

Gloter A, Ingrin J, Bouchet D, Scrivener K, Colliex C (2000b) TEM evidence of perovskite-brownmillerite coexistence in the $Ca(Al_xFe_{1-x})O_{2.5}$ system with minor amounts of titanium and silicon. Phys Chem Miner 27: 504–513

Golla U, Putnis A (2001) Valence state mapping and quantitative electron spectroscopic imaging of exsolution in titanohematite by energy-filtered TEM. Phys Chem Miner 28: 119–129

Höfer HE, Brey GP, Schulz-Dobrick B, Oberhänsli R (1994) The determination of the oxidation state of iron by the electron microprobe. Eur J Mineral 6: 407–418

Höfer HE, Brey GP, Oberhänsli R (1995) The determination of the oxidation state of iron in synthetic garnets by X-ray spectroscopy with the electron microprobe. Phys Chem Miner 23: 241

Höfer HE, Weinbruch S, McCammon CA, Brey GP (2000) Comparison of two electron probe microanalysis techniques to determine ferric iron in synthetic wüstite samples. Eur J Mineral 12: 63–71

King PL, Hervig RL, Holloway JR, Delaney JS, Dyar MD (2000) Partitioning of Fe^{3+}/Fe_{total} between amphibole and basanitic

melt as a function of oxygen fugacity. Earth Planet Sci Lett 178: 97–112

Krishnan KM (1990) Iron L_{23}-near edge fine structure studies. Ultramicroscopy 32: 309–311

Köhler TP, Brey GP (1990) Calcium exchange between olivine and clinopyroxene calibrated as a geothermobarometer for natural peridotes from 2 to 60 kb with applications. Geochim Cosmochim Acta 54: 2375–2388

Kuiper P, Searle BG, Rudolf P, Tjeng LH, Chen CT (1993) X-ray magnetic dichroism of antiferromagnet Fe_2O_3: the orientation of magnetic moments observed by Fe $2p$ X-ray absorption spectroscopy. Phys Rev Lett 70: 1549–1552

Langenhorst F, van Aken PA (2000) La spectroscopie de perte d'énergie des électrons: principes, techniques et applications. Bull Liaison SFMC 12: 29–38

Lauterbach S, McCammon CA, van Aken P, Langenhorst F, Seifert F (2000) Mössbauer and ELNES spectroscopy of $(Mg,Fe)(Si,Al)O_3$ perovskite: a highly oxidised component of the lower mantle. Contrib Mineral Petrol 138: 17–26

Leapman RD, Grunes LA, Fejes PL (1982) Study of the L_{23} edges in the $3d$ transition-metals and their oxides by electron energy-loss spectroscopy with comparisons to theory. Phys Rev(B) 26: 614–635

Liebscher B (2000) Quantitative Bestimmung der Konzentration von dreiwertigem Eisen mittels Elektronen-Energieverlust-Spektroskopie. PhD thesis Universität Frankfurt 1999. Shaker Verlag, Aachen, ISBN 3-8265-6934-2

Luth RW, Virgo D, Boyd FR, Wood BJ (1990) Ferric iron in mantle-derived garnets. Contrib Mineral Petrol 104: 56–72

Manceau A, Gorshkov AI, Drits VA (1992) Structural chemistry of Mn, Fe, Co, and Ni in manganese hydrous oxides: Part I. Information from XANES spectroscopy. Am Mineral 77: 1133–1143

Marfunin AS (1979) Physics of minerals and inorganic materials: an introduction. Springer, Berlin, Heidelberg, New York, pp 86–87

McCammon CA (1994) A Mössbauer milliprobe: practical considerations. Hyper Inter 92: 1235–1239

McCammon CA, V. Chaskar V, Richards GG (1991) A technique for spatially resolved Mössbauer spectroscopy applied to quenched metallurgical slags. Measurement Sci and Technol 2: 657–662

Menon NK, Yuan J (1998) Quantitative analysis of the effect of probe convergence on electron energy loss spectra of anisotropic materials. Ultramicroscopy 74: 83–94

Menon NK, Yuan J (1999) Towards atomic resolution EELS of anisotropic materials. Ultramicroscopy 78: 185–205

Otten MT, Miner BA, Rask JH, Buseck PR (1985) The determination of Ti, Mn and Fe oxidation states in minerals by electron energy-loss spectroscopy. Ultramicroscopy 18: 285–290

Paterson JH, Krivanek OL (1990) ELNES of $3d$ transition metal oxides. II. Variations with oxidation state and crystal structure. Ultramicroscopy 32: 319–325

Raeburn SP, Ilton ES, Veblen DR (1997a) Quantitative determination of the oxidation state of iron in biotite using X-ray photoelectron spectroscopy: I. Calibration. Geochim Cosmochim Acta 61: 4519–4530

Raeburn SP, Ilton ES, Veblen DR (1997b) Quantitative determination of the oxidation state of iron in biotite using X-ray photoelectron spectroscopy: II. In situ analyzes. Geochim Cosmochim Acta 61: 4531–4537

Redhammer GJ (1996) Untersuchungen zur Kristallphysik von synthetischen Klinopyroxenen im System Hedenbergit-Akmit $CaFe[Si_2O_6]$ – $NaFe[Si_2O_6]$. Dissertation, Naturwissenschaftliche Fakultät, Universität Salzburg

Redhammer GJ, Amthauer G, Lottermoser W, Treutmann W (2000) Synthesis and structural properties of clinopyroxenes of the hedenbergite $(CaFe^{2+}Si_2O_6)$-aegirine $(NaFe^{3+}Si_2O_6)$ solid-solution series. Eur J Mineral 12: 105–120

Schofield PF, van der Laan G, Henderson CMB, Cressey G (1998) A single-crystal, linearly polarized Fe $2p$ X-ray absorption study of gillespite. Mineral Mag 62: 65–75

Spear FS (1995) Metamorphic phase equilibria and pressure-temperature time paths. Mineralogical Society of America, Washington, DC, p 799, Monograph 1

Sutton SR, Delaney JS, Bajt S, Rivers ML, Smith JV (1993) Microanalysis of iron oxidation state in iron oxides using X-ray absorption near-edge structure (XANES). In: Lunar and planetary science, vol XXIV, Lunar and Planetary Institute, pp 1385–1386

Thole BT, van der Laan G, Sawatzky GA (1985) Strong magnetic dichroism predicted in the $M_{4,5}$ X-ray absorption spectra of magnetic rare-earth materials. Phys Rev Lett 55: 2086–2088

van Aken PA (1995) Use of Fe $L_{2,3}$-edge electron energy-loss spectroscopy to characterize multiple valence states of iron in minerals: a new probe for mineralogical and geochemical research. Ber DMG, Beih Eur J Mineral 7: 255

van Aken PA, Liebscher B, Styrsa VJ (1998) Quantitative determination of iron oxidation states in minerals using Fe $L_{2,3}$-edge electron energy-loss near edge structure spectroscopy. Phys Chem Miner 25: 323–327

van Aken PA, Styrsa VJ, Liebscher BH, Woodland AB, Redhammer GJ (1999) Microanalysis of $Fe^{3+}/\Sigma Fe$ in oxide and silicate minerals by investigation of electron energy-loss near-edge structures (ELNES) at the Fe $M_{2,3}$ edge. Phys Chem Miner 26: 584–590

van der Laan G, Kirkman IW (1992) The $2p$ absorption spectra of $3d$ transition metal compounds in tetrahedral and octahedral symmetry. J Phys Cond Matter 4: 4189–4204

van der Laan G, Thole BT, Sawatzky GA, Goedkoop JB, Fuggle JC, Esteva JM, Karnatak R, Remeika JP, Dabkowska HA (1986) Experimental proof of magnetic X-ray dichroism. Phys Rev(B) 34: 6529–6531

Woodland AB, O'Neill HStC (1993) Synthesis and stability of $Fe_3^{2+}Fe_2^{3+}Si_3O_{12}$ garnet and phase relations with $Fe_3Al_2Si_3O_{12}$–$Fe_3^{2+}Fe_2^{3+}Si_3O_{12}$ solutions. Am Mineral 78: 1002–1015

Woodland AB, Ross II CR (1994) A crystallographic and Mössbauer spectroscopy study of $Fe_3^{2+}Al_2Si_3O_{12}$–$Fe_3^{2+}Fe_2^{3+}Si_3O_{12}$ (almandine–"skiagite") and $Ca_3Fe_2^{3+}Si_3O_{12}$–$Fe_3^{2+}Fe_2^{3+}Si_3O_{12}$ (andradite–"skiagite") garnet solid solutions. Phys Chem Miner 21: 117–132

Woodland AB, O'Neill HStC (1995) Phase relations between $Ca_3Fe_2^{3+}Si_3O_{12}$–$Fe_3^{2+}Fe_2^{3+}Si_3O_{12}$ garnet and $CaFeSi_2O_6$–$Fe_2Si_2O_6$ pyroxene solid solutions. Contrib Mineral Petrol 121: 87–98

Woodland AB, Droop G, O'Neill HStC (1995) Almandine-rich garnet from near Collobrières, southern France, and its petrological significance. Eur J Mineral 7: 187–194